Strongly time-variable ultraviolet metal-line emission from the circum-galactic medium of high-redshift galaxies

Niharika Sravan,[1]* Claude-André Faucher-Giguère,[1] Freeke van de Voort,[2,3] Dušan Kereš,[4] Alexander L. Muratov,[4] Philip F. Hopkins,[5] Robert Feldmann,[2] Eliot Quataert[2] and Norman Murray[6]†

[1]*Center for Interdisciplinary Exploration and Research in Astrophysics (CIERA), and Department of Physics and Astronomy, Northwestern University, 2145 Sheridan Road, Evanston IL 60208, USA*
[2]*Department of Astronomy and Theoretical Astrophysics Center, University of California, Berkeley, CA 94720-3411, USA*
[3]*Academia Sinica Institute of Astronomy and Astrophysics, PO Box 23-141, Taipei 10617, Taiwan*
[4]*Department of Physics, Center for Astrophysics and Space Science, University of California, San Diego, 9500 Gilman Drive, La Jolla, CA 9209, USA*
[5]*TAPIR, Mailcode 350-17, California Institute of Technology, Pasadena, CA 91125, USA*
[6]*Canadian Institute for Theoretical Astrophysics, 60 St. George Street, University of Toronto, ON M5S 3H8, Canada*

ABSTRACT

We use cosmological simulations from the Feedback In Realistic Environments project, which implement a comprehensive set of stellar feedback processes, to study ultraviolet (UV) metal-line emission from the circum-galactic medium of high-redshift ($z = 2$–4) galaxies. Our simulations cover the halo mass range $M_h \sim 2 \times 10^{11}$–$8.5 \times 10^{12}$ M$_\odot$ at $z = 2$, representative of Lyman break galaxies. Of the transitions we analyse, the low-ionization C III (977 Å) and Si III (1207 Å) emission lines are the most luminous, with C IV (1548 Å) and Si IV (1394 Å) also showing interesting spatially extended structures. The more massive haloes are on average more UV-luminous. The UV metal-line emission from galactic haloes in our simulations arises primarily from collisionally ionized gas and is strongly time variable, with peak-to-trough variations of up to $\sim$2 dex. The peaks of UV metal-line luminosity correspond closely to massive and energetic mass outflow events, which follow bursts of star formation and inject sufficient energy into galactic haloes to power the metal-line emission. The strong time variability implies that even some relatively low-mass haloes may be detectable. Conversely, flux-limited samples will be biased towards haloes whose central galaxy has recently experienced a strong burst of star formation. Spatially extended UV metal-line emission around high-redshift galaxies should be detectable by current and upcoming integral field spectrographs such as the Multi Unit Spectroscopic Explorer on the Very Large Telescope and Keck Cosmic Web Imager.

Key words: galaxies: evolution – galaxies: formation – galaxies: high-redshift – galaxies: haloes – intergalactic medium – cosmology: theory.

1 INTRODUCTION

In the cosmic web, galaxies form in dark matter overdensities. In order to sustain star formation across cosmic time, they continuously accrete their baryonic fuel from the surrounding intergalactic medium along with dark matter (IGM; Kereš et al. 2005; Prochaska & Wolfe 2009; Bauermeister, Blitz & Ma 2010; Faucher-Giguère, Kereš & Ma 2011). Some of this gas is later returned to the circum-galactic medium (CGM), along with metals produced in stars, via powerful galactic winds driven by feedback from stars (e.g. Aguirre

et al. 2001; Springel & Hernquist 2003; Oppenheimer & Davé 2006; Martin et al. 2010; Rubin et al. 2010; Steidel et al. 2010) and active galactic nuclei (AGNs; e.g. Fabjan et al. 2010; Wiersma, Schaye & Theuns 2011). Since the inflows and outflows that regulate galaxy formation are mediated through the CGM, measurements of the gas properties in the CGM are a powerful approach to understanding galaxy assembly and evolution.

To date, most of our observational constraints on the physical state of the CGM have come from absorption line studies. Absorption lines have the advantage that even low-density, faint gas can be probed if there is a suitable background source. Absorption line measurements however have several imitations. First, suitable background sources (typically, quasars) are rare so that there is typically only one (or no) background sight line per foreground

* E-mail: niharika@u.northwestern.edu
† Canada Research Chair in Astrophysics.

galaxy (e.g. Adelberger et al. 2005a; Prochaska & Hennawi 2009; Rudie et al. 2012; Tumlinson et al. 2013). Because the area covered scales as the square of the impact parameter, the resulting measurements preferentially probe large impact parameters from foreground galaxies. Finally, because of the 1D nature of absorption line constraints it is often unclear what physical structures are probed.[1]

Integral field measurements of emission lines are complementary to absorption line measurements. In particular, they allow us to directly obtain a 3D picture of the distribution of gas in the CGM by combining the 2D map of emission on the sky with line-of-sight velocity information. In recent years, we have indeed learned a great deal about spatially resolved kinematics of high-redshift galaxies using this technique (e.g. Genzel et al. 2008; Förster Schreiber et al. 2009; Law et al. 2009; Wright et al. 2009). Additionally, since gas emissivity scales with the square of density, emission line studies preferentially probe the dense gas closer to galaxies. To date, it has generally not been possible to make 3D emission line maps of the CGM of galaxies because halo gas is much fainter than galactic gas, thus pushing the capabilities of existing astronomical instruments. The situation is however changing thanks to efforts to build sensitive integral field spectrographs (IFSs) that are well suited to detect the low surface brightness (SB) features expected from inflows and outflows around galaxies.

Thanks to the abundance of hydrogen, H I Lyman-α (Ly α) is the most easily detectable line from the CGM. Our first glimpses of the CGM emission have come from spatially extended Ly α sources known as 'Ly α blobs' (LABs). The blobs have line luminosities up to $\sim 10^{44}$ erg s^{-1} and spatial extents sometimes exceeding 100 proper kpc (Steidel et al. 2000; Matsuda et al. 2004; Yang et al. 2009). The physical nature of LABs is not yet well understood but there is growing evidence that they are often powered by an energetic source such as an AGN or a starburst galaxy (which can be beamed away from the line of sight and appear obscured; Geach et al. 2009, 2014; Prescott et al. 2015). AGN and star-forming galaxies can induce the CGM to glow through several mechanisms. Ly α photons can be produced inside galaxies by the processing of ionizing photons that are absorbed by the interstellar medium (ISM) and scatter in a diffuse halo as they escape the galaxy. Diffuse Ly α haloes are now inferred to be generically produced by ordinary star-forming galaxies by this mechanism (Steidel et al. 2011). Ionizing photons that escape galaxies but are absorbed in the CGM can also produce fluorescent Ly α emission (e.g. Gould & Weinberg 1996; Cantalupo et al. 2005; Kollmeier et al. 2010). Alternatively, energy can be injected in the CGM as galactic winds driven by stellar or AGN feedback encounter halo gas. This energy can then power Ly α emission from the CGM (Taniguchi & Shioya 2000; Taniguchi, Shioya & Kakazu 2001). We indeed show in this paper that galactic winds can power significant metal-line emission from circum-galactic gas, and that this process induces dramatic time variability. Finally, spatially extended Ly α emission can be powered by gravitational potential energy that is dissipated as gas falls into dark matter haloes (Haiman, Spaans & Quataert 2000; Fardal et al. 2001; Dijkstra & Loeb 2009; Goerdt et al. 2010; Rosdahl & Blaizot 2012). Calculations that take into account self-shielding of dense

gas suggest however that gravity-driven Ly α emission is in general too faint to explain the most luminous LABs (Faucher-Giguère et al. 2010).

In spite of a growing body of high-quality observations of spatially extended Ly α at high-redshift (e.g. Rauch et al. 2008; Hennawi et al. 2009; Cantalupo et al. 2014; Martin et al. 2014a), these observations have proved difficult to interpret because of the strong radiative transfer effects experienced by Ly α photons as they are scattered by interstellar and circum-galactic gas (e.g. Dijkstra, Haiman & Spaans 2006; Verhamme, Schaerer & Maselli 2006; Faucher-Giguère et al. 2010). In effect, scattering scrambles the photons both spatially and spectrally, making it challenging to reliably infer the geometry and kinematics of the emitting gas.

Emission from metal lines in the CGM can be powered by the same physical processes as Ly α. Because metals are not as abundant, metal-line emission is generally fainter and more difficult to detect than Ly α. Observing metal lines however provides valuable complementary information, and in some respects provide a more direct window into the physics of circum-galactic gas flows. Most metal lines are optically thin and therefore not subject to significant photon scattering, unlike Ly α. Furthermore, different metal ions probe different temperature regimes, allowing us to construct a more complete physical picture. In particular, ions with high ionization potential preferentially probe more diffuse, volume-filling gas whereas Ly α emission tends to peak around cold filaments (e.g. Faucher-Giguère et al. 2010; Goerdt et al. 2010; Rosdahl & Blaizot 2012). Since much of the cooling of the diffuse universe occurs through rest-frame ultraviolet (UV) emission (e.g. Bertone, Aguirre & Schaye 2013), rest-UV metal lines offer a powerful way to probe galaxy formation. Rest-frame UV from $z \sim 2$–4, covering the peak of the cosmic star formation history (e.g. Bouwens et al. 2007), also has the benefit of being redshifted into the optical and thus is accessible using large optical telescopes.

A number of optical IFSs with the capacity to detect low SB, redshifted rest-UV CGM emission have recently been commissioned or are planned for the near future. The Cosmic Web Imager (CWI; Matuszewski et al. 2010) started taking data on the Hale 200" telescope at Palomar Observatory in 2009 and the first science results on luminous spatially extended Ly α sources at $z \sim 2 - 3$ have recently been reported (Martin et al. 2014a,b). Its successor, the Keck Cosmic Web Imager[2] (KCWI, Martin et al. 2010), to be mounted on the Keck II telescope at the W. M. Keck Observatory on Mauna Kea, is currently being developed. The Multi Unit Spectroscopic Explorer[3] (MUSE; Bacon et al. 2010) on the Very Large Telescope (VLT) completed its commissioning in 2014 August and early science results are being reported (e.g. Fumagalli et al. 2014; Bacon et al. 2015; Richard et al. 2015; Wisotzki et al. 2016). MUSE combines a wide field of view, excellent spatial resolution, and a large spectral range. These IFSs not only provide kinematic information not available with narrow-band imaging but also enable more accurate background subtraction to characterize low SB features.

Cosmological simulations have previously been used to predict UV emission from the IGM and the CGM (e.g. Furlanetto et al. 2004; Bertone et al. 2010; Frank et al. 2012; Bertone & Schaye 2012; van de Voort & Schaye 2013). Our simulations, from the FIRE (Feedback In Realistic Environments) project,[4] improve on these previous analyses in several respects. Most of our zoom-in

---

[1] With the advent of 30-m class optical telescopes, it will become possible to sample galaxy haloes more densely by using ordinary galaxies as background sources (e.g. Steidel et al. 2010). With sufficiently dense sampling, absorption line measurements can produce 3D tomographic maps of the foreground gas.

[2] http://www.srl.caltech.edu/sal/keck-cosmic-web-imager.html

[3] http://muse.univ-lyon1.fr

[4] See the FIRE project web site at: http://fire.northwestern.edu.

simulations have a gas particle mass of a few times 10^4 M$_\odot$ and a minimum (adaptive) gas gravitational softening length of ∼10 proper pc. For comparison, the highest resolution simulations from the OWLS project analysed by van de Voort & Schaye (2013) have a gas particle mass of 2.1×10^6 M$_\odot$ and a maximum gas gravitational softening length of 700 proper pc (see also Bertone & Schaye 2012). The high resolution of our zoom-ins allows us to resolve the main structures in the ISM of galaxies. Our simulations also explicitly treat stellar feedback from supernovae of Types I and II, stellar winds from young and evolved stars, photoionization, and radiation pressure on dust grains.

Our suite of simulations has been shown to successfully reproduce the observationally inferred relationship between stellar mass and dark matter halo mass (the $M_\star - M_h$ relation; Hopkins et al. 2014) and the mass–metallicity relations (Ma et al. 2016) of galaxies below ∼$L^\star$ at all redshifts where observational constraints are currently available, as well as the covering fractions of dense HI in the haloes of $z = 2 - 4$ Lyman break galaxies (LBGs) and quasars (Faucher-Giguère et al. 2015; Faucher-Giguère et al. 2016). In these simulations, we find that star formation histories and the resultant galactic winds are highly time variable (Muratov et al. 2015; Sparre et al. 2015), a property that we show in this paper induces corresponding time variability in the UV emission from circum-galactic gas. Unlike in some more ad hoc stellar feedback implementations, our simulations follow hydrodynamical interactions and gas cooling at all times, lending some credence to the phase structure of galactic winds predicted in our calculations.

Our primary goal in this paper is to investigate the implications of the high resolution and explicit stellar feedback models of the FIRE simulations for UV metal-line emission from the CGM of high-redshift galaxies and its physical origin. Our analysis is guided by the UV metal lines most likely to be detectable by MUSE and KCWI, though it is beyond the scope of this paper to make detailed observational predictions for specific instruments.

This paper is organized as follows. We describe our simulations in more detail and our methodology for computing metal-line emission in Section 2. We present our main results in Section 3, including a discussion of the strong predicted stellar feedback-driven UV metal-line time variability. We summarize our conclusions in Section 4. The Appendices contain a convergence test and local source test.

2 METHODOLOGY

2.1 Simulations

Here we summarize the numerical methods used in our simulations and the physics included. For more details on the algorithms, we refer the reader to Hopkins et al. (2014) and references therein.

Our simulations were run with the GIZMO code (Hopkins 2015) in 'P-SPH' mode. P-SPH, described in Hopkins (2013), is a Lagrangian-based pressure–entropy formulation of the smooth particle hydrodynamics (SPH) equations that eliminates some of the well-known differences between traditional implementations of SPH and grid-based codes (e.g. Agertz et al. 2007; Sijacki et al. 2012) while preserving the excellent conservation properties of SPH. GIZMO derives from GADGET-3 (last described in Springel 2005) and its tree particle-mesh (TREEPM) gravity solver is based on the latter. Our GIZMO runs include improved algorithms and prescriptions for artificial viscosity (Cullen & Dehnen 2010), entropy mixing (Price 2008), adaptive time stepping (Durier & Dalla Vecchia 2012), the smoothing kernel (Dehnen & Aly 2012), and adaptive

Table 1. Parameters of the simulations analysed in this work.

Name	$M_h^{z=2}$ (M$_\odot$)	m_b (M$_\odot$)	ϵ_b (pc)	m_{dm} (M$_\odot$)	ϵ_{dm} (pc)
m12v	2.0×10^{11}	3.9×10^4	10	2.0×10^5	140
m12q	5.1×10^{11}	7.1×10^3	10	2.8×10^5	140
m12i	2.7×10^{11}	5.0×10^4	14	2.8×10^5	140
m13	8.7×10^{11}	3.7×10^5	20	2.3×10^6	210
z2h830	5.4×10^{11}	5.9×10^4	9	2.9×10^5	143
z2h650	4.0×10^{11}	5.9×10^4	9	2.9×10^5	143
z2h600	6.7×10^{11}	5.9×10^4	9	2.9×10^5	143
z2h550	1.9×10^{11}	5.9×10^4	9	2.9×10^5	143
z2h506	1.2×10^{12}	5.9×10^4	9	2.9×10^5	143
z2h450	8.7×10^{11}	5.9×10^4	9	2.9×10^5	143
z2h400	7.9×10^{11}	5.9×10^4	9	2.9×10^5	143
z2h350	7.9×10^{11}	5.9×10^4	9	2.9×10^5	143
MFz2_B1	8.5×10^{12}	3.3×10^4	9	1.7×10^5	143

Parameters describing the initial conditions for our simulations (units are physical).
(1) Name: simulation designation. Simulations **mx** have a main halo mass ∼10^x M$_\odot$ at $z = 0$.
(2) $M_h^{z=2}$: mass of the main halo at $z = 2$.
(3) m_b: initial baryonic (gas and star) particle mass in the high-resolution region.
(4) ϵ_b: minimum baryonic force softening (fixed in physical units past $z \sim 10$; minimum SPH smoothing lengths are comparable or smaller). Force softening lengths are adaptive (mass resolution is fixed).

gravitational softening (Price & Monaghan 2007; Barnes 2012). Star formation in the FIRE simulations only occurs in molecular, self-gravitating gas with $n_H \gtrsim 5$–50 cm^{-3}. The energy, momentum, mass, and metal yields from photoionization, radiation, stellar winds and supernovae are calculated using STARBURST99 (Leitherer et al. 1999). The abundances of nine metallic species (C, N, O, Ne, Mg, Si, S, Ca, and Fe) are also tracked using this method and used to evaluate cooling rates using a method similar to Wiersma, Schaye & Smith (2009). Ionization balance of these elements are computed assuming the cosmic ionizing background of Faucher-Giguère et al. (2009) (FG09).[5] Self-shielding of hydrogen is accounted for with a local Jeans-length approximation (integrating the local density at a given particle out to a Jeans length to determine a surface density Σ), then attenuating the background seen at that point by $e^{-\kappa \Sigma}$ (where κ is the opacity). Confirmation of the accuracy of this approximation in radiative transfer experiments can be found in Faucher-Giguère et al. (2010).

The simulations analysed in this work are listed in Table 1. The initial conditions for **m13**, **m12q**, and **m12i** were chosen to match ones from the AGORA project (Kim et al. 2014). The initial conditions for **m12v** are the same as the 'B1' run studied by Kereš & Hernquist (2009) and Faucher-Giguère & Kereš (2011). The **z2hxxx** series of simulations, first described in Faucher-Giguère et al. (2015), consists of haloes in the mass range $M_h = 1.9 \times 10^{11}$ M$_\odot - 1.2 \times 10^{12}$ M$_\odot$ at $z = 2$. These haloes are representative of ones hosting LBGs at that redshift, though somewhat on the low-mass end of the mass distribution (LBGs at $z \sim 2$ reside in dark matter haloes of average mass $M_h \sim 10^{12}$ M$_\odot$; Adelberger et al. 2005b; Trainor & Steidel 2012). **MFz2_B1** is part of the Massive-FIRE simulation suite (Feldmann et al. in preparation). Our simulations do not include feedback from AGN. While such feedback may be potentially important, especially in the more massive haloes,

---

[5] Publicly available at http://galaxies.northwestern.edu/uvb.

Table 2. UV Lines analysed in this work.

Ion Name	λ_1 (Å)	λ_2 (Å)	MUSE		KCWI	
			z_{min}	z_{max}	z_{min}	z_{max}
C IV	1548	1551	2.00	5.01	1.26	5.78
Si IV	1394	1403	2.34	5.67	1.51	6.53
N V	1239	1243	2.75	6.51	1.82	7.47
O VI	1032	1038	3.51	8.01	2.39	9.17
Si III	1207	–	2.85	6.71	1.90	7.70
C III	977	–	3.76	8.52	2.58	9.75

(1) λ_1: rest-frame wavelength of the emission line or the stronger line for doublets.

(2) λ_2: rest-frame wavelength of the weaker line for doublets.

(3) z_{min}: the minimum redshift from which the stronger transition line lies within the wavelength coverage of MUSE and KCWI.

(4) z_{max}: the maximum redshift from which the stronger transition line lies within the wavelength coverage of MUSE and KCWI.

Note: the wavelength coverage of MUSE and KCWI are 4650–9300 Å and 3500–10 500 Å, respectively.

the proper modelling of AGN feedback is still a major theoretical challenge (e.g. Somerville & Davé 2015) and we have decided to postpone its treatment to future work. We focus our analysis on main haloes (i.e. we do not centre on satellite haloes). The SB profiles of UV line emission may, however, include emission contributed by satellite galaxies. Haloes are identified using Amiga's Halo Finder (Knollmann & Knebe 2009) and we adopt the virial overdensity definition of Bryan & Norman (1998).

All our simulations assume a 'standard' flat ΛCDM cosmology with $h \approx 0.7$, $\Omega_m = 1 - \Omega_\Lambda \approx 0.27$ and $\Omega_b \approx 0.046$. Minor variations about these fiducial values are adopted for some simulations to match the parameters of simulations from the AGORA project and from our previous work. Uncertainties in our calculations are dominated by baryonic physics and the small variations in cosmological parameters do not introduce significant effects in our analysis.

2.2 Emissivity calculation

Our method for calculating gas emissivities is similar to the one used by van de Voort & Schaye (2013).

Following previous work that identified the most important contributions to rest-UV emission from the high-redshift CGM (Bertone & Schaye 2012; van de Voort & Schaye 2013), we compute emissivities for UV doublets C IV (1548 Å, 1551 Å), Si IV (1394 Å, 1403 Å), N V (1239 Å, 1243 Å), and O VI (1032 Å, 1038 Å), and the singlets Si III (1207 Å) and C III (977 Å). We do not show predictions for the Ne VIII (770 Å, 780 Å) doublet because its intrinsic CMG luminosity is ∼3–4 dex below the C III line and suffers from Lyman continuum absorption by the IGM. We do not expect that this line will be observable in the near future. For each doublet, we report only predictions for the strongest line in the doublet. For these doublets, the ratio of the intensity of the stronger and weaker lines in the doublet is ≈2. Therefore, the total intensity for the doublet (e.g. as would be measured by an instrument that does not spectrally resolve the two transitions) can be obtained by multiplying the intensities predicted by a factor of ≈1.5. Table 2 lists the emission lines we study and the minimum and maximum redshifts at which they lie within the wavelength coverage of MUSE and KCWI. We first precompute grids of line emissivities as a function of gas temperature and hydrogen number density over the redshift interval $z = 2$–4 using CLOUDY (version 13.03 of the code last described by Ferland

et al. 2013). The grids sample temperatures in the range $10 < T < 10^{9.5}$ K in intervals of $\Delta \log_{10} T = 0.05$ and hydrogen number densities in the range $10^{-8} < n_H < 10^4$ cm^{-3} in intervals of $\Delta \log_{10} n_H = 0.2$. The grids are computed at redshift intervals of $\Delta z = 0.1$. For the grids, the gas is assumed to be of solar metallicity, optically thin and in photoionization equilibrium with the cosmic ionizing background (the contribution of collisional ionization to equilibrium balance is automatically included). In computing emissivities from our simulations, we bi-linearly interpolate the pre-computed grids in logarithmic space and scale linearly with the actual metallicity of the gas. For most of our calculations, we use the cosmic ionizing background model of Faucher-Giguère et al. (2009); we show in Section 3.1 that the choice of ionizing background model and photoionization from local sources affect our predictions only weakly, indicating that most of the UV emission from metal lines in the CGM originates from regions that are collisionally ionized (see also van de Voort & Schaye 2013).

Non-equilibrium ionization and cooling effects (e.g. Gnat & Sternberg 2007; Oppenheimer & Schaye 2013) are not captured in the present calculations.

2.3 Surface brightness calculation

In order to make full use of the spatially adaptive resolution of our Lagrangian SPH simulations, we evaluate line luminosities from the particle data directly. For a given gas particle, the luminosity of each line listed in Table 2 is calculated as

$$L_{part} = \epsilon_\odot(z, n_H, T) \left(\frac{m_{gas}}{\rho_{gas}} \right) \left(\frac{Z_{gas}}{Z_\odot} \right), \tag{1}$$

where m_{gas}, ρ_{gas}, and Z_{gas} are the mass, density and metallicity of the gas particle, respectively, and $\epsilon_\odot(z, n_H, T)$ is the emissivity interpolated from the pre-computed solar-metallicity grid. This approach for evaluating emissivities is based on total gas metallicity and assumes that the line emitting gas has solar abundance ratios. Our SPH simulations do not include a model for metal diffusion by unresolved turbulence (e.g. Shen, Wadsley & Stinson 2010). While this could potentially cause the metals in the simulations to be too clumped and artificially enhance our predicted luminosities, our simulations do capture the mixing of metals due to resolved gas flows. In Appendix A, we present a convergence test showing that our predicted luminosities do not increase significantly with increasing resolution (and hence increased metal mixing).

To produce SB profiles, we assign particle luminosities to 3D Cartesian grids. The flux from each grid cell is given by

$$F_{cell} = \frac{L_{cell}}{4\pi d_L^2}, \tag{2}$$

where d_L is the luminosity distance and $L_{cell} = \sum L_{part}$ is the sum of the particle luminosities assigned to the cell. The cell side length of the grids is 1 proper kpc for all simulations. This introduces smoothing on that spatial scale (corresponding to 0.1 arcsec at $z = 2$) but does not bias the SB calculations since luminosities are computed from the un-degraded particle-carried information. Finally, the SB projected on the sky is calculated by dividing the flux from each grid cell by the solid angle Ω_{cell} it subtends and summing along the line of sight (los):

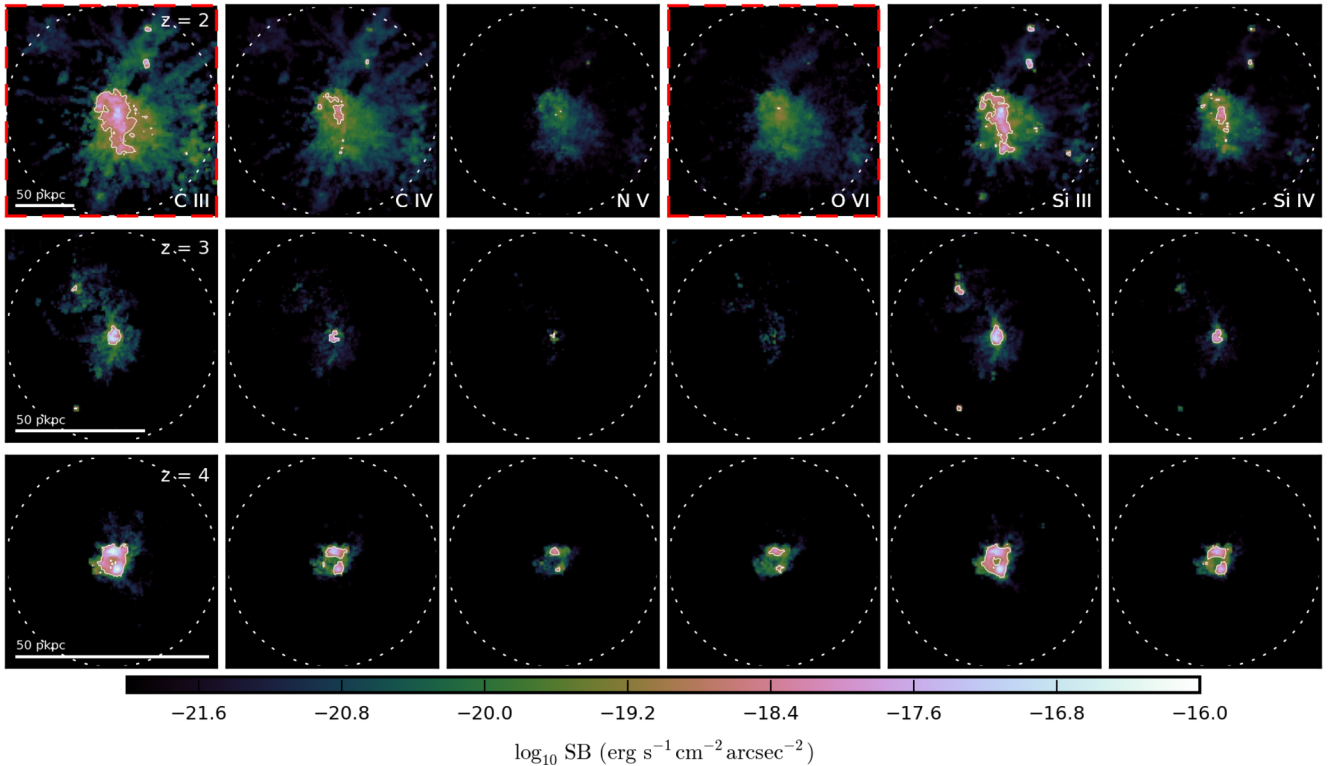$$SB = \sum_{los} \frac{F_{cell}}{\Omega_{cell}}. \tag{3}$$

Figure 1. Theoretical surface brightness (SB) maps for the UV metal lines studied in this work in **z2h506** in a region with side length equal to a virial radius at $z = 2$ (top), 3 (middle), and 4 (bottom). The halo mass in $\log_{10}M_{\rm h}$ (M$_\odot$) is 12.06 ($z = 2$), 11.36 ($z = 3$), and 11.11 ($z = 4$). From left to right, the vertical panels at each redshift show the emission for the C III, C IV, N V, O VI, Si III, and Si IV lines listed in Table 2. The dashed lines show the virial radius in each panel. The solid white contours enclose regions with SB $>10^{-19}$ erg s^{-1} cm^{-2} arcsec^{-2}, a proxy for the SB detectable in (deep but non-stacked) MUSE and KCWI observations. All the emission lines shown would redshift into either the MUSE or KCWI spectral ranges, except C III and O VI at $z = 2$ (indicated by dashed red borders around the panels). The observed SB for the C III, Si III, and O VI lines is subject to IGM attenuation (10–20 per cent, 30–50 per cent, and factor of 2–5 effects at $z = 2$, 3, and 4, respectively; Section 2.4).

In the small angle limit and for cubical grid cells, $\Omega_{\rm cell} = (a_{\rm cell}/d_{\rm A})^2$, where $a_{\rm cell}$ is the proper side length of a grid cell and $d_{\rm A}$ is the angular diameter distance.

2.4 IGM attenuation

Absorption by intervening intergalactic gas affects the detectability of the emission lines we predict (e.g. Madau 1995). The emission lines we analyse in this paper all have rest wavelength $\lambda > 912$ Å and so are not affected by Lyman continuum opacity. The C III, Si III, and O VI emission lines that we consider however have rest wavelengths $\lambda < 1216$ Å and so will be attenuated by Lyman-series opacity. Using the IGM attenuation model of Inoue et al. (2014), we calculated the transmission factor e$^{-\tau}$ for the C III 977 Å, Si III 1207 Å, and O VI 1032 Å lines. For these three lines, we find transmission factors (0.9, 0.8, 0.9) at $z = 2$, (0.7, 0.5, 0.7) at $z = 3$, and (0.5, 0.2, 0.4) at $z = 4$, respectively. Thus, IGM attenuation has a small effect on our predictions at $z = 2$. Even out to $z = 4$, IGM attenuation is only a factor of ~ 2 effect for C III and O VI. While significant, this is much smaller than the order-of-magnitude time variability that our simulations predict (see Section 3.2), so this does not significantly affect any of our main conclusions. At $z = 4$, the IGM may suppress observable Si III emission by a factor of ~ 5, which will make this line more challenging to detect at such redshifts. The C IV, N V, and S IV lines we analyse do not suffer from Lyman-series absorption and so are not significantly affected by hydrogen absorption from the IGM. To allow readers to easily correct our results for other

IGM attenuation models (proximity effects could be important for Si III 1207 Å, which has a rest wavelength close to Ly α 1216 Å), in this paper we plot theoretical SBs taking into account cosmological dimming but neglecting IGM attenuation.

3 RESULTS

3.1 UV metal-lines maps and radial profiles

Figs 1 and 2 show SB maps for the UV metal lines in Table 2 for **z2h506** and **MFz2_B1**, respectively. These are our two most massive haloes at $z = 2$. In these maps, solid white contours enclose regions with SB $>10^{-19}$ erg s^{-1} cm^{-2} arcsec^{-2}, a proxy for the SB detectable in (deep but non-stacked) MUSE and KCWI observations. High-redshift Lyα CGM emission has been detected in narrow-band imaging observations down to $\sim 10^{-18}$ erg s^{-1} cm^{-2} arcsec^{-2} in individual objects (Steidel et al. 2000; Matsuda et al. 2004) and down to $\sim 10^{-19}$ erg s^{-1} cm^{-2} arcsec^{-2} in stacks (Steidel et al. 2011). Current and upcoming IFSs such as MUSE and KCWI are expected to reach an order of magnitude deeper. For reference, SB $= 10^{-19}$ erg s^{-1} cm^{-2} arcsec^{-2} is the 1σ detection threshold for the azimuthally averaged Lyα radial profiles in the recent ultra-deep exposure in the Hubble Deep Field South obtained with MUSE (Wisotzki et al. 2016). Comparing Figs 1 ($M_{\rm h} = 1.2 \times 10^{12}$ M$_\odot$ at $z = 2$) and 2 ($M_{\rm h} = 8.5 \times 10^{12}$ M$_\odot$ at $z = 2$) suggests a significant halo mass dependence for the detectability of metal UV lines, with the more massive halo showing more spatially extended
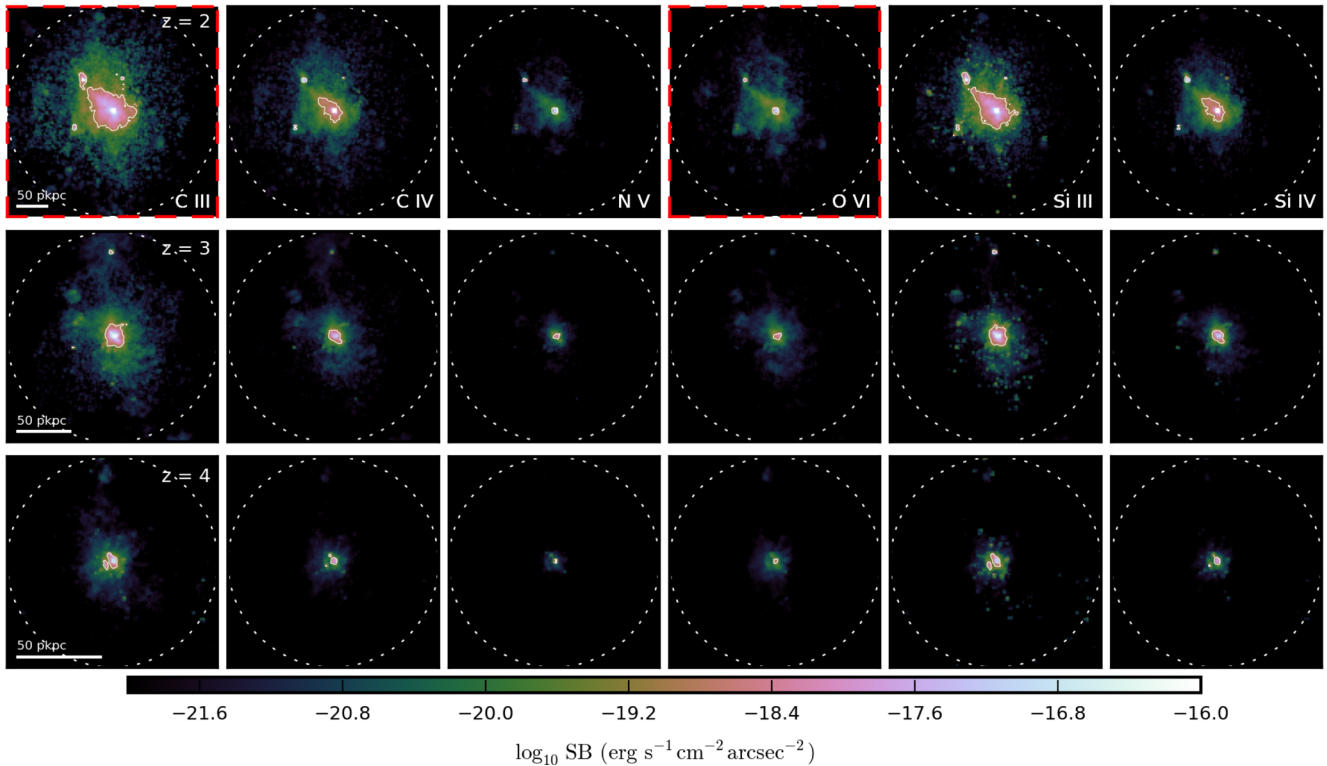
Figure 2. Same as in Fig. 1 but for the more massive halo **MFz2_B1**. The halo mass in $\log_{10} M_h$ (M$_\odot$) is 12.93 ($z = 2$), 12.52 ($z = 3$), and 12.21 ($z = 4$).

and more luminous emission (note the different spatial scales). In Section 3.2, we will show that the CGM UV metal-line emission is primarily powered by energy injection from galactic winds. Since more massive haloes on average have higher star formation rates (before quenching), these haloes are naturally more luminous *on average*.

For **MFz2_B1**, the C III and Si III lines are predicted to produce emission above 10^{-19} erg s^{-1} cm^{-2} arcsec^{-2} on spatial scales ∼100 proper kpc (in the elongated direction) at $z = 2$, and C IV and Si IV should be detectable at this SB on scales ∼50 proper kpc. For **z2h506**, we predict similar structures but with spatial extent smaller by approximately the ratio of the virial radius in **z2h506** relative to that of **MFz2_B1** (a factor of ≈0.5 at $z = 2$). These transitions preferentially probe relatively cool, $T \sim 10^{4.5} - 10^5$ K gas. All these lines would redshift into either the MUSE or KCWI spectral bands if observed from $z = 2 - 4$, except C III at $z \sim 2$. In Fig. 3, we show the median and mean radial SB profiles[6] for all the haloes in our sample but excluding **MFz2_B1** (which is of substantially higher mass than the rest). O VI (which preferentially probes warmer gas, $T \sim 10^{5.5}$ K gas) is less luminous than C IV and Si IV by ∼1 dex and does not redshift into the KCWI and MUSE bands at $z = 2$. O VI emission may be detectable at higher redshifts in very deep integrations of massive haloes but could prove beyond the reach of the current generation of instruments. As we show in Section 3.2, UV emission from the CGM is highly time variable. Therefore, different haloes of the same mass and at the same redshift may produce very different circum-galactic UV metal emission profiles.

The metal UV line emission from our simulated haloes is generally easier to detect at $z \sim 2$ than at $z \sim 3 - 4$. Two effects contribute to this. First, our haloes grow with time and their star formation rates also on average increase with time over that redshift interval (e.g. Hopkins et al. 2014; Muratov et al. 2015), thus increasing the amount of energy injected in the CGM and radiated by the UV lines. Secondly, the SB is subject to cosmological SB dimming, $SB \propto (1 + z)^{-4}$. Note that the virial radii of the simulated haloes in Fig. 3 increase with decreasing redshift so that the total luminosities of the $z = 2$ haloes are systematically higher even though the SB at a fixed fraction of R_{vir} appears to follow a different redshift trend.

The different rows in Fig. 3 correspond to different assumptions for the ionizing flux illuminating CGM gas. The top row assumes our fiducial FG09 UV/X-ray background. To test the sensitivity to the shape of the ionizing spectrum, we have repeated our CLOUDY emissivity calculations using the Haardt & Madau (2005, private communication) background, which we rescaled by a factor of 0.447 to match the hydrogen photoionization rate $\Gamma_{HI} = 5.5 \times 10^{-13}$ s^{-1} of the FG09 model at $z = 3$ (middle row). We also tested the sensitivity of our results to the magnitude of the ionizing flux by multiplying the FG09 background by a factor of 10 (bottom row). The mean and average SB profiles are almost identical between the different rows, at $z = 2, 3$ and 4, indicating that our predictions are not sensitive to the assumed ionizing background model. This implies that the UV metal-line emission arises primarily from collisionally ionized gas whose ionization state is not sensitive to the ionizing flux, as previously found by van de Voort & Schaye (2013). Furthermore, the metal-line emission that we focus on arises primarily from gas at temperatures $T \sim 10^{4.5} - 10^6$ K, which is generally collisionally heated. We have verified that our simulations predict emissivity-weighted temperatures broadly consistent with fig. 6 of van de Voort & Schaye (2013). This implies that self-shielding effects do not significantly affect our UV
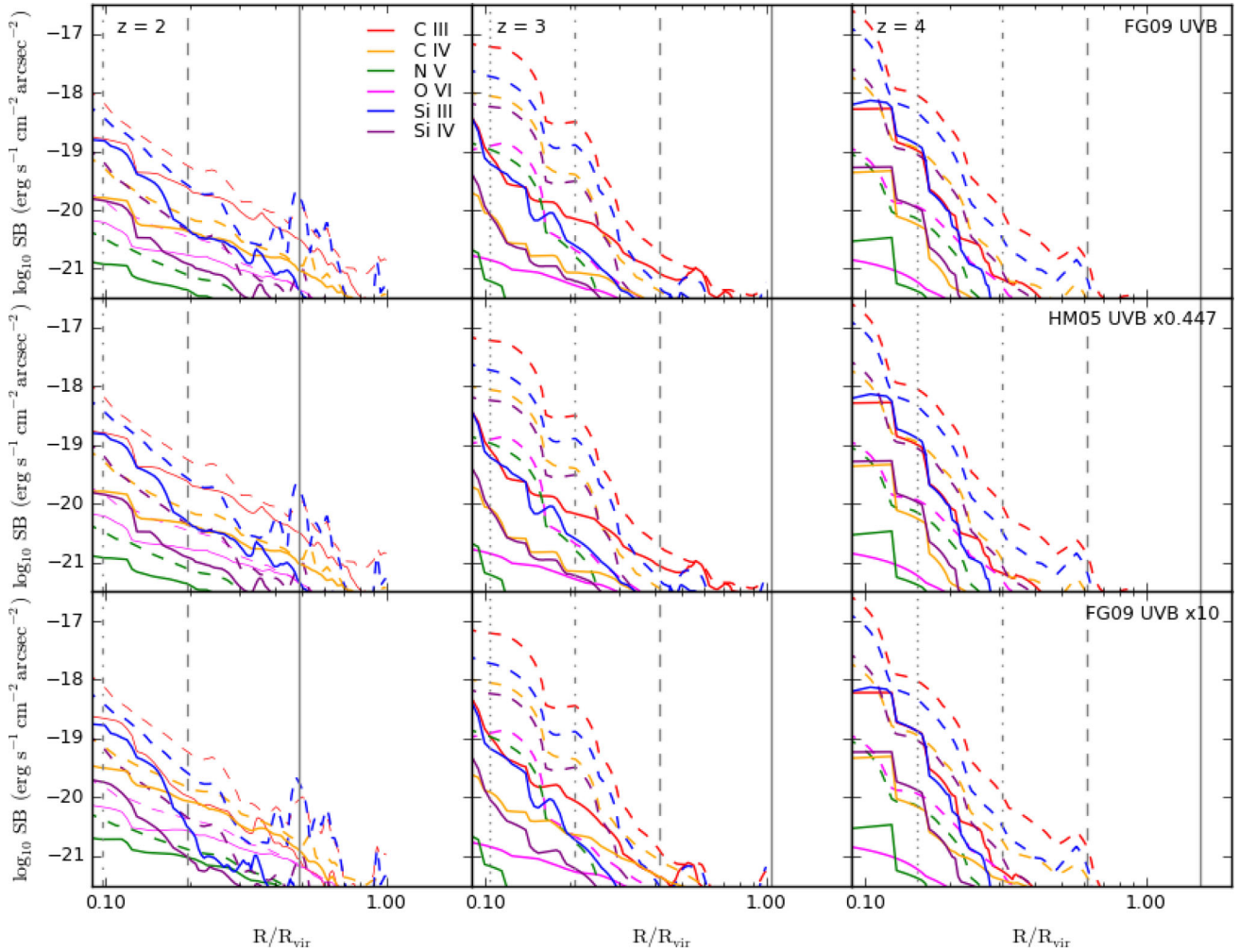
[6] To calculate the average mean and median radial profiles, we first compute the cylindrically averaged profiles for individual haloes, then take the mean and median over haloes in our sample. To compute the cylindrical averages, the radial profiles are radially binned in bins of width 3 proper kpc.

Figure 3. Median (solid lines) and mean (dotted lines) UV metal-line theoretical radial surface brightness (SB) profiles for the sample of Lyman break galaxy simulations described in Section 2.1 (excluding **MFz2_B1**) at $z = 2$ (left), 3 (middle), and 4 (right), assuming the FG09 UV/X-ray ionizing background model (top), the galaxy+quasar HM05 UV/X-ray background scaled by a factor of 0.447 (to match the hydrogen photoionization rate of the FG09 model at $z = 3$; middle), and the FG09 background multiplied by a factor of 10 (bottom). The mean and median halo masses in $\log_{10} M_{\rm h}$ (M$_\odot$) are 11.79 and 11.82 ($z = 2$), 11.44 and 11.40 ($z = 3$), and 11.11 and 11.10 ($z = 4$), respectively. The vertical dotted, dot–dashed, dashed and solid grey lines indicate radii of 5, 10, 20, and 50 proper kpc for median-mass haloes at each redshift. SB profiles shown with thinner curves correspond to emission lines that do not redshift into the MUSE or KCWI bands (indicated by the dashed red border panels in Figs 1 and 2). The observed SB for the C III, Si III, and O VI lines is subject to IGM attenuation (10–20 per cent, 30–50 per cent, and factor of 2–5 effects at $z = 2$, 3, and 4, respectively; Section 2.4).

metal-line emission, unlike for Ly α emission for which self-shielding effects are critical (e.g. Faucher-Giguère et al. 2010). This experiment also indicates that ionizing photons emitted by local galaxies (which we have neglected) likely would not substantially alter our predictions. Measurements of the fraction of ionizing photons that escape the ISM of LBGs at $z \sim 3$ moreover indicate that $f_{\rm esc} \sim 5$ per cent (e.g. Shapley et al. 2006). If this fraction corresponds to the fraction of directions along which ionizing photons escape relatively unimpeded, and the ISM is opaque to ionizing photons along other directions, most of the CGM around star-forming galaxies is not strongly illuminated by the central galaxy. In Appendix B, we present another test explicitly including a local source spectrum (including X-rays from supernova remnants) that also shows that our main predictions are not significantly affected by local sources (though some details of the line emission at low SBs are).

To give a sense of how our predictions vary from halo to halo, Fig. 4 shows the predicted cylindrically averaged radial SB profiles for a representative sample of individual haloes (**MFz2_B1**, **z2h506**,

and **z2h450**). The spikes in the radial profiles (for example, at $R/R_{\rm vir} \sim 0.5$ for **MFz2_B1** at $z = 2$) are due to satellite galaxies (see the maps in Figs 1 and 2).

Our predicted average SB profiles shown in the top panels of Fig. 3 agree with those obtained by van de Voort & Schaye (2013) from the OWLS simulations to within ~ 0.5 dex on average (with no apparent systematic differences). However, we find that the intensities of UV metal lines vary by several dex from halo to halo. Furthermore, there is strong variability in the strength of individual metal lines between haloes of otherwise similar mass and redshift. For example, the strength of C III in **z2h506** and **z2h450** at $z = 4$ differ by ~ 3 dex in SB, even though both haloes have a mass $M_{\rm h} \approx 10^{11.1}$ M$_\odot$ at that redshift. We address this in the next section.

3.2 Star formation-driven time variability

One of the key predictions of the FIRE simulations with resolved ISM is that the star formation histories of galaxies have a
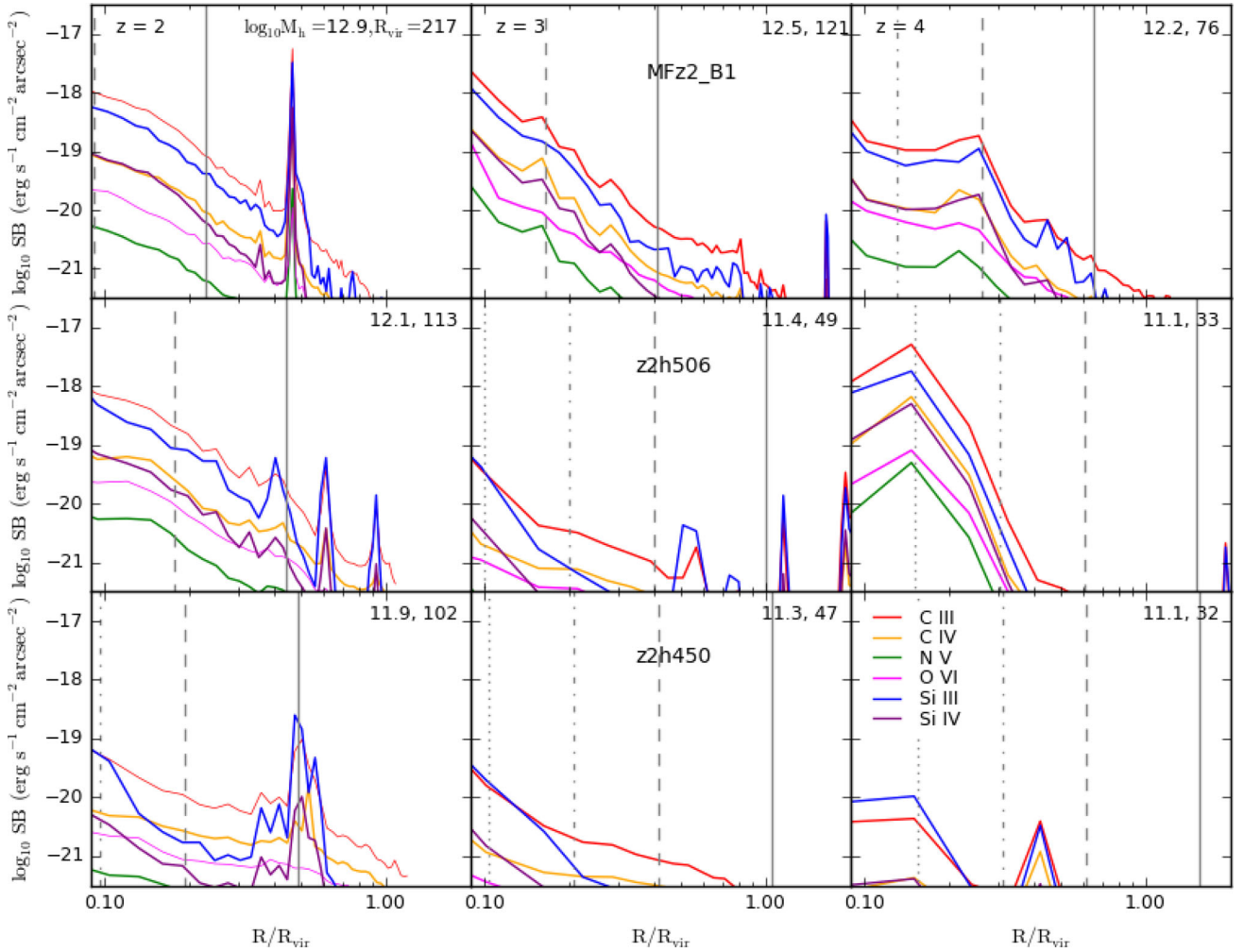
Figure 4. Cylindrically averaged UV metal-line radial theoretical surface brightness (SB) profiles for haloes **MFz2_B1** (top), **z2h506** (middle), and **z2h450** (bottom) at $z = 2$ (left), 3 (middle), and 4 (right). Values of $\log_{10} M_h (M_\odot)$ and R_{vir} (proper kpc) for each halo are indicated at the top right of each panel. The vertical dotted, dot–dashed, dashed and solid grey lines indicate radii of 5, 10, 20, and 50 proper kpc, respectively. SB profiles shown with thinner curves correspond to emission lines that do not redshift into the MUSE or KCWI bands (indicated by the dashed red border panels in Figs 1 and 2). The observed SB for the C III, Si III, and O VI lines is subject to IGM attenuation (10–20 per cent, 30–50 per cent, and factor of 2–5 effects at $z = 2, 3$, and 4, respectively; Section 2.4).

strong stochastic component and are much more time variable (e.g. Hopkins et al. 2014; Sparre et al. 2015) than in lower resolution simulations in which the ISM is modelled with a sub-grid effective equation of state. Such sub-grid equations of state are standard in current large-volume cosmological simulations (e.g. Davé et al. 2013; Vogelsberger et al. 2014; Schaye et al. 2015). In particular, a sub-grid equation of state was used in the OWLS simulations analysed by van de Voort & Schaye (2013) for UV line emission from the CGM. We have previously shown that the time variability of star formation in the FIRE simulations results in time variable galactic winds (Muratov et al. 2015), an increased cool gas content of galaxy haloes (Faucher-Giguère et al. 2015), and can transform dark matter halo cusps into cores in dwarf galaxies (Oñorbe et al. 2015; Chan et al. 2015). Similar time variability has also been found in other zoom-in simulations implementing different stellar feedback models (Governato et al. 2010; Guedes et al. 2011; Stinson et al. 2013; Agertz & Kravtsov 2015), indicating that it is a generic consequence of resolving the ISM of galaxies, in which local dynamical time-scales can be very short. We now show that time-variable star formation also has important implications for the observability of

CGM gas in emission, and explains why two haloes of the same mass and redshift can vary in metal UV line luminosity by orders of magnitude.

In Fig. 5 we plot the luminosities of UV metal lines within $1R_{vir}$ (a proxy for emission from central galaxies), for **z2h506** and **z2h450**, as a function of redshift. We also plot the star formation rates within $1R_{vir}$ and gas mass outflow rates at $0.25R_{vir}$ in these haloes as a function of redshift. As the Figure shows, the UV metal-line luminosities, star formation rates, and mass outflow rates all exhibit strong and correlated time variability. In particular, epochs of peak metal-line emission coincide closely with massive outflow events in the haloes (though some outflow events do not result in strongly enhanced UV line emission), with peak-to-trough variations of up to ~2 dex in luminosity. It is noteworthy that peaks in UV line luminosities correspond more closely with peaks in mass outflow rate than with peaks in star formation rate. In the FIRE simulations, star formation rate peaks typically precede mass outflow rate (and UV line luminosity) by ≈60 Myr, corresponding to the travel time from the galaxy to $0.25R_{vir}$ (Muratov et al. 2015). This indicates that while metal UV line emission time variability is ultimately
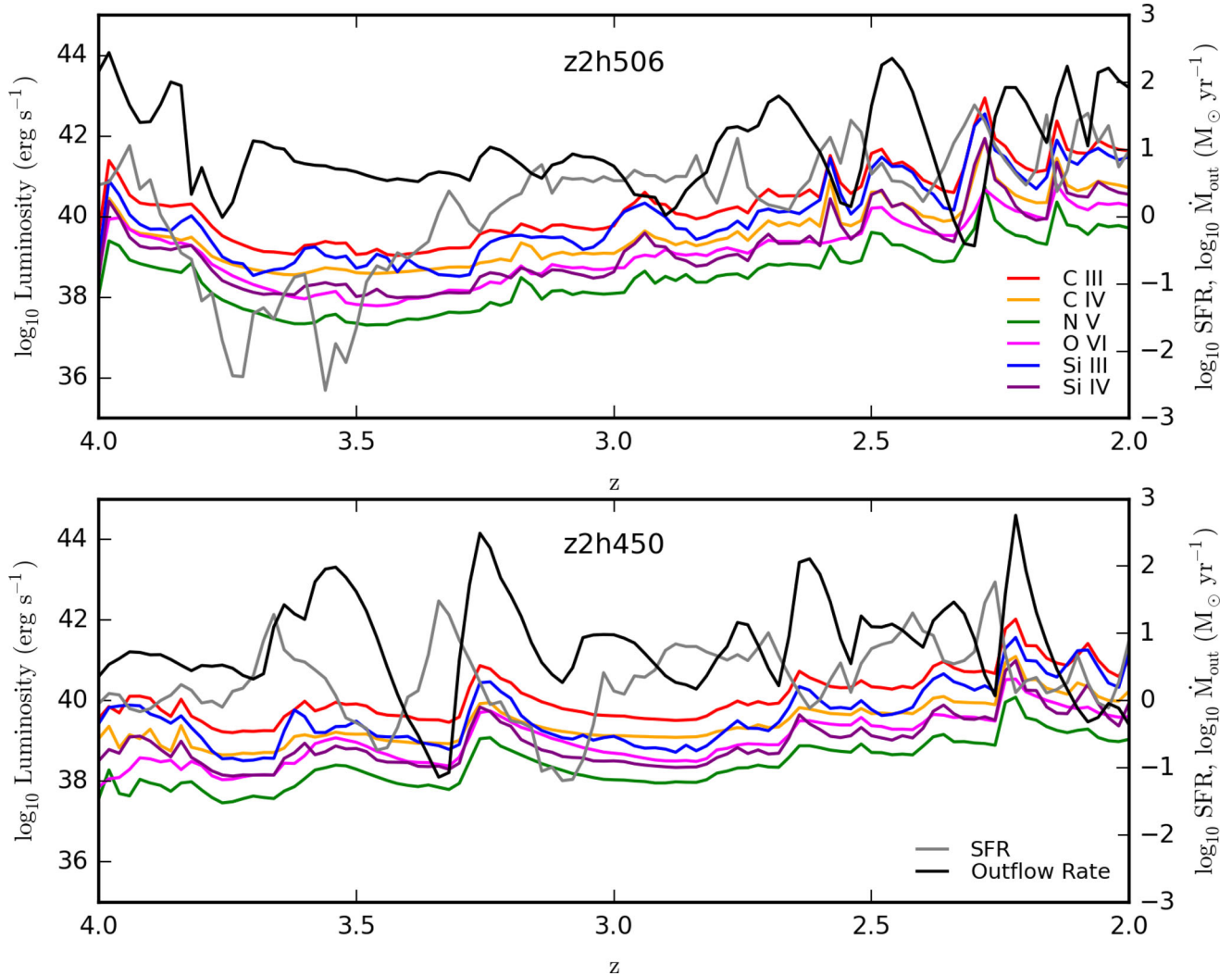
Figure 5. Coloured lines show UV metal-line luminosities within $1\,R_{\rm vir}$ but excluding the inner 10 proper kpc (a proxy for central galaxies) in simulated haloes **z2h506** (top) and **z2h450** (bottom) as a function of redshift. Star formation rates within $1\,R_{\rm vir}$ and gas mass outflow rates at $0.25\,R_{\rm vir}$ as a function of redshift are plotted as grey and black lines, respectively. The UV metal-line luminosities, star formation, and mass outflow rates are all strongly time variable and correlated. Peaks in CGM luminosity correspond more closely with peaks in mass outflow rates, which follow peaks of star formation with a time delay, indicating that energy injected in the haloes by galactic winds powers the UV metal-line emission.

driven by star formation time variability, it is the star formation-driven galactic winds specifically that inject energy into the CGM, which is ultimately radiated away by UV metal lines (among other channels). This finding is consistent with our conclusion in the previous section that the UV metal-line emission arises primarily in collisionally ionized gas, with little sensitivity to the ionizing flux. The kinetic energy carried by an outflow with mass outflow rate $\dot{M}_{\rm out}$ and velocity $v_{\rm w}$ is

$$\dot{E}_{\rm w} \equiv \frac{1}{2}\dot{M}_{\rm out}v_{\rm w}^2 \tag{4}$$

$$\approx 3 \times 10^{42}\ {\rm erg\ s}^{-1}\left(\frac{\dot{M}_{\rm out}}{100\,{\rm M}_\odot\,{\rm yr}^{-1}}\right)\left(\frac{v_{\rm w}}{300\,{\rm km\ s}^{-1}}\right)^{1/2}, \tag{5}$$

which is sufficient to power the predicted UV metal-line emission [see Muratov et al. (2015) for measurements of outflow velocities in our simulations]. Fig. 5 explains why halo **z2h506** is much more luminous than halo **z2h450** at $z = 4$ in spite of being nearly identical

in mass: at $z \sim 4$, **z2h506** experiences a very massive and energetic mass outflow.

Fig. 6 shows more quantitatively the correlations between CGM UV metal-line luminosities (for the C III and Si III lines, which are generally most luminous), star formation rate, and mass outflow rate. Overall, CGM UV line luminosities correlate positively with mass outflow rate at fixed redshift but no significant correlation with instantaneous star formation rate is apparent. The relationship with instantaneous star formation rate is much weaker because of the time delay between star formation bursts and outflows through $0.25R_{\rm vir}$. This again indicates that energy injection from galactic winds is the primary driver of the emission. Despite the correlation, the relationship between CGM luminosities and outflow rate is not one-to-one (in some redshift intervals, the relationship even appears inverted) because the luminosity is not simply a function of mass outflow rate but also of how the wind energy is dissipated as the wind interacts with other CGM gas. At high redshift, the FIRE simulated haloes are very dynamic, which introduces significant fluctuations in how the wind energy is dissipated. The FIRE
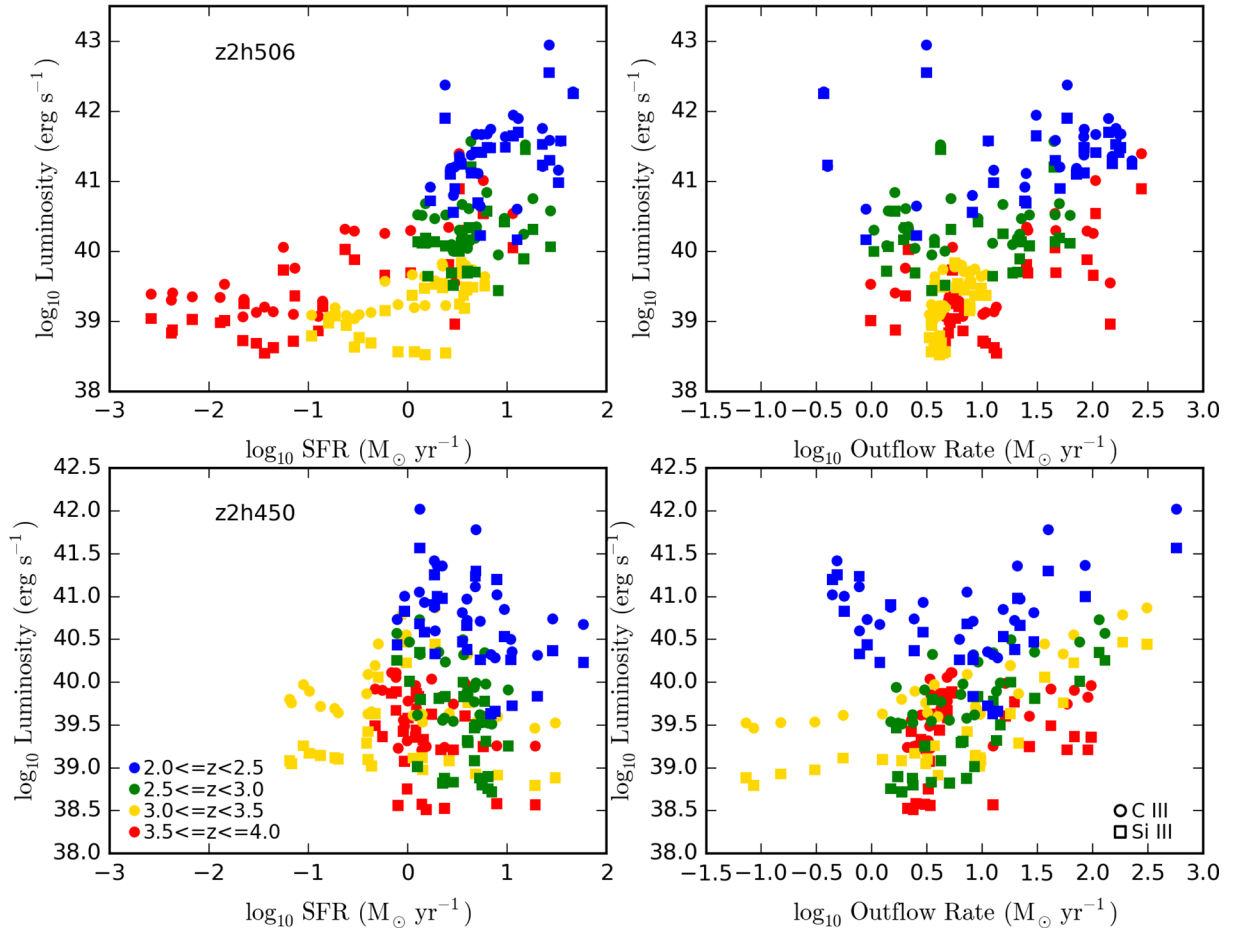
Figure 6. UV metal-line luminosities within $1\,R_{vir}$ but excluding the inner 10 proper kpc of halo centres (a proxy for central galaxies) in simulated haloes **z2h506** (top) and **z2h450** (bottom). The luminosities are plotted versus the star formation rate within R_{vir} (left) and versus the mass outflow rate at $0.25R_{vir}$. Circle symbols show the C III luminosity and square symbols show Si III luminosity. Colours indicate redshift bins (100 time slices between $z = 4$ and $z = 2$ are shown). Overall, CGM UV line luminosities correlate positively with mass outflow rate at fixed redshift but no significant correlation with instantaneous star formation rate is apparent.

simulations predict that star formation rates and outflows both become more time steady at low redshift ($z \lesssim 1$; Muratov et al. 2015), so a tighter relationship between CGM luminosities and star formation rate may result at low redshift. Since the metal-line emissivity scales with gas metallicity (equation 1), another potential source of time variability is fluctuations in gas metallicity. However, the average wind metallicity in our simulations fluctuates by a factor of only ~2 in our simulations (Muratov et al. 2016) so this must be a subdominant effect on the total order-of-magnitude time variability.

There is some support from observations that star formation-driven outflows inject energy into galaxy haloes that can collisionally excite metal lines. Turner et al. (2015) inferred based on ionization modelling of O VI absorption lines coincident with low HI columns the presence of a substantial mass of metal-enriched, $T > 10^5$ K collisionally ionized gas around $z \sim 2.3$ star-forming galaxies, which they identified with hot outflows from the galaxies.

An important implication of the star formation-driven time variability of UV metal lines is that CGM gas could be detected in emission in relatively low-mass haloes which are experiencing strong outbursts. Conversely, detections of CGM emission will in general be biased towards haloes that have recently experienced a burst of star formation followed by an energetic outflow.

4 CONCLUSIONS

Motivated by current and upcoming IFSs on 8–10 m class telescopes, such as MUSE on the VLT and KCWI on Keck, we used cosmological zoom-in simulations from the FIRE project to make predictions for UV metal-line emission from the CGM of $z = 2 - 4$ star-forming galaxies. These simulations resolve the ISM of individual galaxies and implement a comprehensive model of stellar feedback, including photoionization, radiation pressure on dust grains, stellar winds, and supernovae of Types I and II. We analysed 13 simulations with main haloes in the mass range $M_h \sim 2 \times 10^{11} - 8.5 \times 10^{12}$ M$_\odot$ at $z = 2$, representative of LBGs. For each simulation, we predicted the emission from the C III (977 Å), C IV (1548 Å), Si III (1207 Å), Si IV (1394 Å), O VI (1032 Å), and N V (1239 Å) metal lines.

Our results can be summarized as follows.

(i) Of the transitions we analyse, the low-ionization C III (977 Å) and Si III (1207 Å) emission lines are the most luminous, with C IV (1548 Å) and Si IV (1394 Å) also showing interesting spatially extended structures that should be detectable by MUSE and KCWI. At $z \leq 3$, the C III and Si III lines are attenuated by Lyman-series opacity from the IGM by factors of $\lesssim 2$, but at $z = 2$ the Si III line

is expected to be attenuated by a factor of ∼5. The more massive haloes are on average more UV-luminous.

(ii) The UV metal-line emission from galactic haloes in our simulations arises primarily from collisionally ionized gas and is thus weakly sensitive to the ionizing flux, including ionization from local galaxies.

(iii) The UV metal-line emission from galactic haloes in our simulations is strongly time variable, with peak-to-trough variations of up to ∼2 dex. The time variability of UV metal-line emission is driven by the time variable star formation predicted by our resolved ISM simulations, but is most closely correlated with the time variability of gas mass outflow rates measured at $0.25R_{\rm vir}$. Our simulations thus indicate that stellar feedback powers UV metal-line emission through energy injected in haloes by galactic winds.

The prediction that UV metal-line emission arises in gas collisionally excited in outflows could be tested by comparing the emission line kinematics with outflow velocities predicted by the simulations. In the FIRE simulations, the median outflow velocity at $0.25R_{\rm vir}$ scales with the halo circular velocity $v_{\rm c}$ (Muratov et al. 2015). On its own, this test may prove ambiguous since ∼$v_{\rm c}$ is also the velocity expected of gas falling into haloes. Furthermore, kinematic measurements transverse to galaxies cannot in general distinguish inflows and outflows since it is not known whether the emitting gas is in front or behind the galaxy. On the other hand, 'down-the-barrel' absorption spectroscopy of galaxies (e.g. Shapley et al. 2003; Steidel et al. 2010; Martin et al. 2012; Rubin et al. 2014) can unambiguously probe outflows because the absorbing material is known to lie in front of the stars. Thus, correlating outflow kinematics probed by down-the-barrel absorption spectroscopy with circum-galactic UV metal-line emission could help identify the UV metal-line emission with outflows (with the caveat that a significant time delay may separate peaks in CGM emission and absorption, as well the possible collimation of outflows).

In terms of overall luminosity, our average predictions for UV metal lines from the CGM of high-redshift galaxies are broadly consistent with those of van de Voort & Schaye (2013), which were based on the large-volume OWLS simulations. However, the resolved ISM and stellar feedback physics implemented in the FIRE simulations is critical to capture the strong time variability of star formation and the resulting time variability in UV metal-line emission. The strong predicted time variability of UV metal-line emission has important implications for upcoming observations: even some relatively low-mass haloes may be detectable in deep observations with current generation instruments. Conversely, flux-limited samples will be biased towards haloes whose central galaxy has recently experienced a strong burst of star formation.

Our finding that galactic winds power UV metal-line emission from CGM gas is reminiscent of the 'super wind' model for LABs (Taniguchi & Shioya 2000; Taniguchi et al. 2001) and highlights the potential of detecting halo gas in emission for constraining stellar feedback. Our current calculations do not include the effects of AGNs, whose radiative and mechanical interactions with halo gas also likely contribute substantially to metal UV line emission. It is clearly worthwhile to include the effects of AGN in future calculations.

ACKNOWLEDGEMENTS

REFERENCES

Adelberger K. L., Shapley A. E., Steidel C. C., Pettini M., Erb D. K., Reddy N. A., 2005a, ApJ, 629, 636
Adelberger K. L., Steidel C. C., Pettini M., Shapley A. E., Reddy N. A., Erb D. K., 2005b, ApJ, 619, 697
Agertz O., Kravtsov A. V., 2015, ApJ, 804, 18
Agertz O. et al., 2007, MNRAS, 380, 963
Aguirre A., Hernquist L., Schaye J., Weinberg D. H., Katz N., Gardner J., 2001, ApJ, 560, 599
Bacon et al., 2010, in Proc. SPIE Conf. Ser. Vol. 7735, The MUSE second-generation VLT instrument. SPIE, Bellingham
Bacon et al., 2015, A&A, 575, A75
Barnes J. E., 2012, MNRAS, 425, 1104
Bauermeister A., Blitz L., Ma C.-P., 2010, ApJ, 717, 323
Bertone S., Schaye J., 2012, MNRAS, 419, 780
Bertone S., Schaye J., Booth C. M., Vecchia C. D., Theuns T., Wiersma R. P. C., 2010, MNRAS, 408, 1120
Bertone S., Aguirre A., Schaye J., 2013, MNRAS, 430, 3292
Bouwens R. J., Illingworth G. D., Franx M., Ford H., 2007, ApJ, 670, 928
Bryan G. L., Norman M. L., 1998, ApJ, 495, 80
Cantalupo S., 2010, MNRAS, 403, L16
Cantalupo S., Porciani C., Lilly S. J., Miniati F., 2005, ApJ, 628, 61
Cantalupo S., Arrigoni-Battaia F., Prochaska J. X., Hennawi J. F., Madau P., 2014, Nature, 506, 63
Cerviño M., Mas-Hesse J. M., Kunth D., 2002, A&A, 392, 19
Chan T. K., Kereš D., Oñorbe J., Hopkins P. F., Muratov A. L., Faucher-Giguère C.-A., Quataert E., 2015, MNRAS, 454, 2981
Cullen L., Dehnen W., 2010, MNRAS, 408, 669
Davé R., Katz N., Oppenheimer B. D., Kollmeier J. A., Weinberg D. H., 2013, MNRAS, 434, 2645
Dehnen W., Aly H., 2012, MNRAS, 425, 1068
Dijkstra M., Loeb A., 2009, MNRAS, 400, 1109
Dijkstra M., Haiman Z., Spaans M., 2006, ApJ, 649, 14
Durier F., Dalla Vecchia C., 2012, MNRAS, 419, 465
Fabjan D., Borgani S., Tornatore L., Saro A., Murante G., Dolag K., 2010, MNRAS, 401, 1670
Fardal M. A., Katz N., Gardner J. P., Hernquist L., Weinberg D. H., Davé R., 2001, ApJ, 562, 605
Faucher-Giguère C.-A., Kereš D., 2011, MNRAS, 412, L118
Faucher-Giguère C.-A., Lidz A., Zaldarriaga M., Hernquist L., 2009, ApJ, 703, 1416
Faucher-Giguère C.-A., Kereš D., Dijkstra M., Hernquist L., Zaldarriaga M., 2010, ApJ, 725, 633
Faucher-Giguère C.-A., Kereš D., Ma C.-P., 2011, MNRAS, 417, 2982

Faucher-Giguère C.-A., Hopkins P. F., Kereš D., Muratov A. L., Quataert E., Murray N., 2015, MNRAS, 449, 987

Faucher-Giguère C.-A., Feldmann R., Quataert E., Keres D., Hopkins P. F., Murray N., 2016, MNRAS, 461L, 32

Ferland G. J. et al., 2013, Rev. Mex. Astron. Astrofis., 49, 137

Förster Schreiber N. M. et al., 2009, ApJ, 706, 1364

Frank S. et al., 2012, MNRAS, 420, 1731

Fumagalli M., Fossati M., Hau G. K. T., Gavazzi G., Bower R., Sun M., Boselli A., 2014, MNRAS, 445, 4335

Furlanetto S. R., Schaye J., Springel V., Hernquist L., 2004, ApJ, 606, 221

Geach J. E. et al., 2009, ApJ, 700, 1

Geach J. E.et al., 2014, ApJ, 793, 22

Genzel R. et al., 2008, ApJ, 687, 59

Gnat O., Sternberg A., 2007, ApJS, 168, 213

Goerdt T., Dekel A., Sternberg A., Ceverino D., Teyssier R., Primack J. R., 2010, MNRAS, 407, 613

Gould A., Weinberg D. H., 1996, ApJ, 468, 462

Governato F. et al., 2010, Nature, 463, 203

Guedes J., Callegari S., Madau P., Mayer L., 2011, ApJ, 742, 76

Haiman Z., Spaans M., Quataert E., 2000, ApJ, 537, L5

Hennawi J. F., Prochaska J. X., Kollmeier J., Zheng Z., 2009, ApJ, 693, L49

Hopkins P. F., 2013, MNRAS, 428, 2840

Hopkins P. F., 2015, MNRAS, 450, 53

Hopkins P. F., Kereš D., Oñorbe J., Faucher-Giguère C.-A., Quataert E., Murray N., Bullock J. S., 2014, MNRAS, 445, 581

Inoue A. K., Shimizu I., Iwata I., Tanaka M., 2014, MNRAS, 442, 1805

Kereš D., Hernquist L., 2009, ApJ, 700, L1

Kereš D., Katz N., Weinberg D. H., Davé R., 2005, MNRAS, 363, 2

Kim J.-H. et al., 2014, ApJS, 210, 14

Knollmann S. R., Knebe A., 2009, ApJS, 182, 608

Kollmeier J. A., Zheng Z., Davé R., Gould A., Katz N., Miralda-Escudé J., Weinberg D. H., 2010, ApJ, 708, 1048

Law D. R., Steidel C. C., Erb D. K., Larkin J. E., Pettini M., Shapley A. E., Wright S. A., 2009, ApJ, 697, 2057

Leitherer C. et al., 1999, ApJS, 123, 3

Ma X., Hopkins P. F., Faucher-Giguère C.-A., Zolman N., Muratov A. L., Kereš D., Quataert E., 2016, MNRAS, 456, 2140

Madau P., 1995, ApJ, 441, 18

Martin C., Moore A., Morrissey P., Matuszewski M., Rahman S., Adkins S., Epps H., 2010, in Proc. SPIE Conf. Ser. Vol. 7735, The Keck Cosmic Web Imager. SPIE, Bellingham

Martin C. L., Scannapieco E., Ellison S. L., Hennawi J. F., Djorgovski S. G., Fournier A. P., 2010, ApJ, 721, 174

Martin C. L., Shapley A. E., Coil A. L., Kornei K. A., Bundy K., Weiner B. J., Noeske K. G., Schiminovich D., 2012, ApJ, 760, 127

Martin D. C., Chang D., Matuszewski M., Morrissey P., Rahman S., Moore A., Steidel C. C., 2014a, ApJ, 786, 106

Martin D. C., Chang D., Matuszewski M., Morrissey P., Rahman S., Moore A., Steidel C. C., Matsuda Y., 2014b, ApJ, 786, 107

Mas-Hesse J. M., Otí-Floranes H., Cerviño M., 2008, A&A, 483, 71

Matsuda Y. et al., 2004, AJ, 128, 569

Matuszewski M., Chang D., Crabill R. M., Martin D. C., Moore A. M., Morrissey P., Rahman S., 2010, in Proc. SPIE Conf. Ser. Vol. 7735, The Cosmic Web Imager: an integral field spectrograph for the Hale Telescope at Palomar Observatory: instrument design and first results. SPIE, Bellingham

Muratov A. L., Kereš D., Faucher-Giguère C.-A., Hopkins P. F., Quataert E., Murray N., 2015, MNRAS, 454, 2691

Muratov A. L. et al., 2016, preprint (arXiv:1606.09252)

Oñorbe J., Boylan-Kolchin M., Bullock J. S., Hopkins P. F., Kereš D., Faucher-Giguère C.-A., Quataert E., Murray N., 2015, MNRAS, 454, 2092

Oppenheimer B. D., Davé R., 2006, MNRAS, 373, 1265

Oppenheimer B. D., Schaye J., 2013, MNRAS, 434, 1043

Prescott M. K. M., Momcheva I., Brammer G. B., Fynbo J. P. U., Møller P., 2015, ApJ, 802, 32

Price D. J., 2008, J. Comput. Phys., 227, 10040

Price D. J., Monaghan J. J., 2007, MNRAS, 374, 1347

Prochaska J. X., Hennawi J. F., 2009, ApJ, 690, 1558

Prochaska J. X., Wolfe A. M., 2009, ApJ, 696, 1543

Rauch M. et al., 2008, ApJ, 681, 856

Richard J. et al., 2015, MNRAS, 446, L16

Rosdahl J., Blaizot J., 2012, MNRAS, 423, 344

Rubin K. H. R., Weiner B. J., Koo D. C., Martin C. L., Prochaska J. X., Coil A. L., Newman J. A., 2010, ApJ, 719, 1503

Rubin K. H. R., Prochaska J. X., Koo D. C., Phillips A. C., Martin C. L., Winstrom L. O., 2014, ApJ, 794, 156

Rudie G. C. et al., 2012, ApJ, 750, 67

Schaye J. et al., 2015, MNRAS, 446, 521

Shapley A. E., Steidel C. C., Pettini M., Adelberger K. L., 2003, ApJ, 588, 65

Shapley A. E., Steidel C. C., Pettini M., Adelberger K. L., Erb D. K., 2006, ApJ, 651, 688

Shen S., Wadsley J., Stinson G., 2010, MNRAS, 407, 1581

Sijacki D., Vogelsberger M., Kereš D., Springel V., Hernquist L., 2012, MNRAS, 424, 2999

Somerville R. S., Davé R., 2015, ARA&A, 53, 51

Sparre M., Hayward C. C., Feldmann R., Faucher-Giguère C.-A., Muratov A. L., Kereš D., Hopkins P. F., 2015, preprint (arXiv:1510.03869)

Springel V., 2005, MNRAS, 364, 1105

Springel V., Hernquist L., 2003, MNRAS, 339, 289

Steidel C. C., Adelberger K. L., Shapley A. E., Pettini M., Dickinson M., Giavalisco M., 2000, ApJ, 532, 170

Steidel C. C., Erb D. K., Shapley A. E., Pettini M., Reddy N., Bogosavljević M., Rudie G. C., Rakic O., 2010, ApJ, 717, 289

Steidel C. C., Bogosavljević M., Shapley A. E., Kollmeier J. A., Reddy N. A., Erb D. K., Pettini M., 2011, ApJ, 736, 160

Stinson G. S., Brook C., Macciò A. V., Wadsley J., Quinn T. R., Couchman H. M. P., 2013, MNRAS, 428, 129

Taniguchi Y., Shioya Y., 2000, ApJ, 532, L13

Taniguchi Y., Shioya Y., Kakazu Y., 2001, ApJ, 562, L15

Trainor R. F., Steidel C. C., 2012, ApJ, 752, 39

Tumlinson J. et al., 2013, ApJ, 777, 59

Turner M. L., Schaye J., Steidel C. C., Rudie G. C., Strom A. L., 2015, MNRAS, 450, 2067

van de Voort F., Schaye J., 2013, MNRAS, 430, 2688

Verhamme A., Schaerer D., Maselli A., 2006, A&A, 460, 397

Vogelsberger M. et al., 2014, MNRAS, 444, 1518

Wiersma R. P. C., Schaye J., Smith B. D., 2009, MNRAS, 393, 99

Wiersma R. P. C., Schaye J., Theuns T., 2011, MNRAS, 415, 353

Wisotzki et al., 2016, A&A, 587A, 98

Wright S. A., Larkin J. E., Law D. R., Steidel C. C., Shapley A. E., Erb D. K., 2009, ApJ, 699, 421

Yang Y., Zabludoff A., Tremonti C., Eisenstein D., Davé R., 2009, ApJ, 693, 1579

APPENDIX A: CONVERGENCE TEST

We test the convergence of our predictions for the intensity of metal emission lines with respect to the resolution of the SPH calculation. To do this we use three versions of the **m12i** simulation: one having a 'fiducial resolution' (the one analysed in the main text and listed in Table 1), one having a 'low resolution' (with a gas particle mass eight times larger and a minimum gas softening length five times larger), and one having a 'high resolution' (with a gas particle mass eight times smaller but same minimum softening). The 'high resolution' version was not evolved all the way to $z = 2$ due to its high computational cost; the figure shows this simulation only to $z = 2.6$. We also use another version of this halo whose parameters are similar to the 'fiducial resolution' version but in which the normalization of the artificial conductivity (entropy mixing parameter) is multiplied by a factor of 4.

In Fig. A1 we plot the C III luminosity within a virial radius as a function of redshift in all four realizations of the **m12i** halo
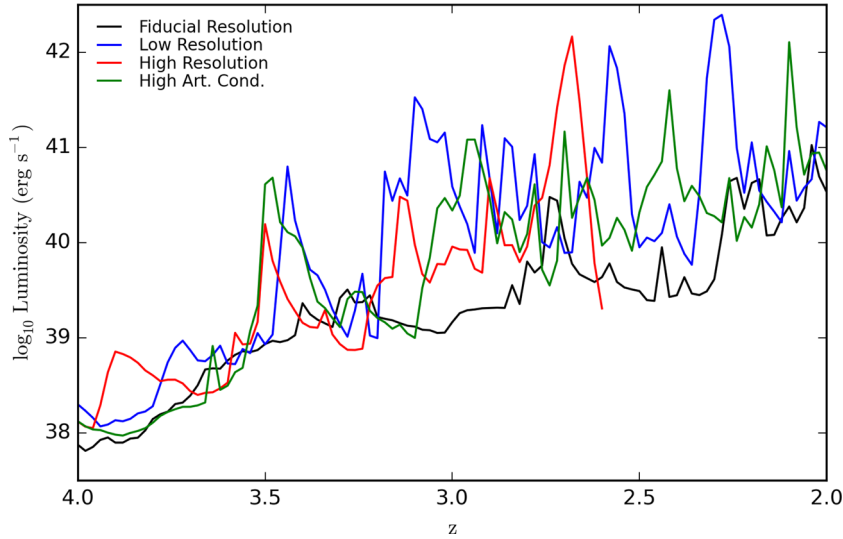
Figure A1. Convergence test for the predicted C III luminosity for **m12i** with respect to the simulation resolution and the artificial conductivity normalization. We plot the C III luminosity within a virial radius as a function of redshift for the fiducial resolution (analysed in the main text), for a lower resolution run, for a higher resolution run (stopped at an earlier redshift), and for fiducial resolution run with the normalization of artificial conductivity multiplied by a factor of 4 (see the text for more details). Accounting for the stochasticity of the simulations, we conclude that the predicted C III luminosity does not depend systematically on resolution or on the normalization of the artificial conductivity, and thus that our predictions are reasonably converged for our fiducial resolution simulations.

described above. In this calculation we have excluded a region of 10 proper kpc centred on the haloes as a proxy for removing emission from the galaxy. Consistent with the results found in Section 3.2, the luminosities for all four realizations are highly time-variable. Accounting for the stochasticity of the simulations, we conclude that the predicted C III luminosity does not depend systematically on resolution or on the normalization of the artificial conductivity, and thus that our predictions are reasonably converged for our fiducial resolution simulations.

APPENDIX B: LOCAL SOURCE TEST

To further test the sensitivity of our CGM emission predictions to local sources of ionizing radiation, we repeated our calculations explicitly including a local source spectrum in addition to the FG09

cosmic background. Specifically, we added a local source spectrum from Cerviño, Mas-Hesse & Kunth (2002) that includes X-ray emission from supernova remnants following Cantalupo (2010). To emphasize the effects of local sources, we chose a relatively high normalization for the local source spectrum corresponding to a distance of 10 proper kpc from a solar-metallicity galaxy with a star formation rate of 100 $M_\odot$ yr^{-1}. We assume that a fraction 5 per cent of the mechanical energy from the starburst is converted into ISM heating and X-ray emission (Mas-Hesse, Otí-Floranes & Cerviño 2008). We assume that all the X-rays escape the galaxy but an escape fraction of 5 per cent for the softer ionizing photons between 1 and 4 Ry. Fig. B1 shows the results of this test and compares them with calculations including only the FG09 background (left) and only the FG09 background but with normalization multiplied by a factor of 10 (right). For SBs $>10^{-20}$ erg s^{-1} cm^{-2} arcsec^{-2}
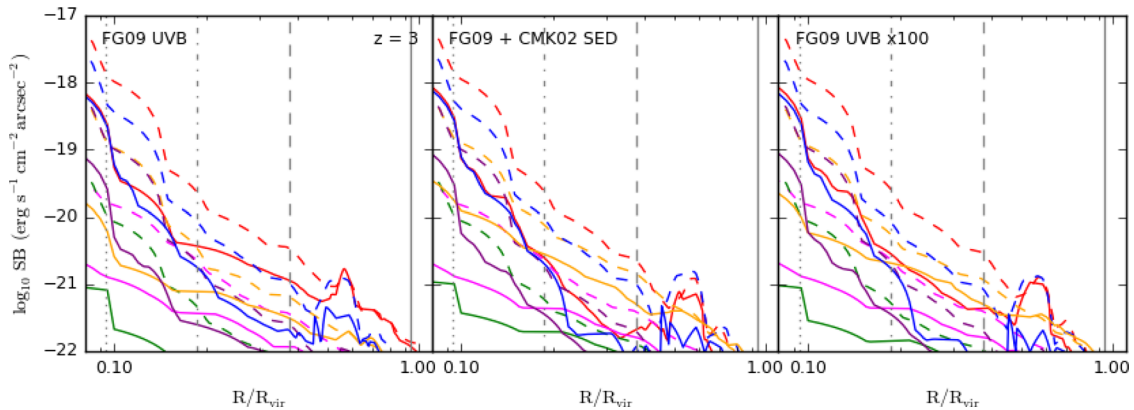

Figure B1. Test of the effects of a local source including X-rays on theoretical surface brightness (SB) profiles. We compare the median (solid) and mean (dashed) SB profiles for five haloes (**z2h506**, **z2h450**, **z2h400**, **z2h830**, and **m12q**) at $z = 3$. Left: profiles including only the FG09 cosmic ionizing background (default in main text). Middle: profiles including the sum of the FG09 background and a local source spectrum from Cerviño et al. (2002), which includes the contribution of supernova remnants to X-rays. The normalization of the X-ray contribution is set to the value expected at 10 proper kpc from a galaxy with a star formation rate of 100 $M_\odot$ yr^{-1}. Right: profiles including only the FG09 background but with normalization boosted by a factor of 10. The mean and median halo masses in $\log_{10}M_h$ ($M_\odot$) are 11.46 and 11.44, respectively. The vertical dotted, dot–dashed, dashed and solid grey lines indicate radii of 5, 10, 20, and 50 proper kpc for the median mass.

potentially observable in deep and stacked observations with MUSE and KCWI, there is no significant difference between the different ionization models. At lower SBs, some differences are noticeable with the inclusion of a local ionizing source. In particular, the C III line is suppressed at large radii while the C IV line is enhanced. However, at those very low SBs, our test overestimates the magnitude of the effect since we do not model the $\propto R^{-2}$ drop off of the

local flux with radius. The effects are seen also in the calculation in which we simply boosted the cosmic UV background, indicating that it is primarily due to the enhancement of relatively soft ionizing photons rather than X-rays from local supernova remnants.

This paper has been typeset from a TeX/LaTeX file prepared by the author.